Volume 1 | Number 1 | Jan 2013 | Pages 1–100

ChemComm

Chemical Communications
www.rsc.org/chemcomm

ROYAL SOCIETY OF CHEMISTRY

ROYAL SOCIETY OF CHEMISTRY

www.rsc.org/chemcomm

Journal Name

ARTICLE TYPE

Segregated Pt on Pd Nanotubes for Enhanced Oxygen Reduction Activity in Alkaline Electrolyte[†]

Samuel St. John,[a] Robert W. Atkinson, III,[a] Ondrej Dyck,[a] Cheng-Jun Sun,[b] Thomas A. Zawodzinski, Jr.,[a,c] and Alexander B. Papandrew[a‡]

Nanoscaled Pt domains were integrated with Pd nanotubes via vapor deposition to yield a highly active electrocatalyst for the oxygen reduction reaction (ORR) in alkaline media. The surface-area-normalized ORR activity of these bi-metallic Pt-on-Pd nanotubes (PtPdNTs) was nearly 6x the corresponding carbon-supported Pt nanoparticle (Pt/C) activity at 0.9 V vs. RHE (1.5 vs. 0.24 mA/cm$^2_{metal}$, respectively). Furthermore, the high specific activity of the PtPdNTs was achieved without sacrificing mass-normalized activity, which is more than twice that of Pt/C (0.333 A/mg$_{PtPdNT}$ vs. 0.141 A/mg$_{Pt/C}$) and also greater than that of Pd/C (0.221 A/mg$_{Pd/C}$). We attribute the enhancements in specific and mass activity to modifications of the segregated Pt electronic structure and to nanoscale porosity, respectively.

Alkaline anion-exchange membrane fuel cells (AAEMFCs) potentially offer significant advantages over proton-exchange membrane fuel cells, including a less corrosive environment, membranes resistant to fouling by dissolved cations, and the availability of highly active metal catalysts outside the platinum group.[1,2] Alkaline cells also promise entirely metal-free cathode catalysts,[3] but the production of peroxide on these carbon-based materials may be problematic[2,4,5]. Metallic catalysts remain the material of choice for the near future of AAEMFCs. Of these, Pd is exceptionally active[6,7] and is resistant to corrosion in the alkaline environment.[8] The departure from the unsatisfactory performance of Pd in acid is owed to subtle changes with respect to reactant/product

binding energy,[9] pH-dependent coverage of oxides and spectator species,[6,10,11] and the role of water as catalytic promoter[12].

Research into the ORR in both acidic and alkaline electrolyte has yielded a blueprint for tuning the reactant/product binding strength for the development of highly active catalysts.[6,9,13] Overlayers atop well-defined bulk crystals[14–27] have been used to enhance the activity of catalysts in comparison to their monometallic constituents for many important reactions using many different synthesis techniques[28–35]. Notably in the alkaline case, Lima et al. demonstrated a volcano-like dependence of ORR specific activity upon the calculated metal d-band center of bulk single-crystal electrodes in alkaline electrolyte,[6] finding optimum activity for Pt monolayers atop Pd(111).

In this contribution, we use an accessible and scalable technique to synthesize segregated Pt domains adorning nanotubes of bulk-like, polycrystalline Pd (PtPdNTs). The nanotube form factor, demonstrated by our group previously for several important electrochemical reactions, has several advantages with respect to previous demonstrations. These advantages include high surface-normalized activity coupled with high mass-normalized activity attributed to the nanoscale porosity within the tube wall.[36,37]

PtPdNT morphology is consistent with the shapes of the pore interiors of the AAO templates in which they were grown, as illustrated using the low magnification HR-TEM in Fig. 1. The nanotubes are approximately 250 nm in diameter, matching the average diameter of the AAO templates, with variable lengths ~10 μm. At higher magnification (Fig. 1b-e) fine nanoscale porosity is observed. Wall thicknesses in these samples are approximately 25-30 nm. Larger variations in grain size have been achieved with different heat treatment temperatures[36] and can be optimized depending upon the catalytic application. Heat treatment in a reducing atmosphere removes interstitial carbon from the Pd lattice absorbed during synthesis[38] and promotes sintering and relaxation of the aggregated nanoparticles formed during vapor deposition into durable, highly coordinated structures.

PtPdNTs display an fcc crystal structure. There is evidence of

[a] Department of Chemical and Biomolecular Engineering, University of Tennessee, Knoxville, TN, USA.
[b] X-ray Science Division, Argonne National Laboratory, Argonne, IL, USA.
[c] Materials Science and Technology Division, Oak Ridge National Laboratory, Oak Ridge, TN, USA.
[†] Electronic Supplementary Information (ESI) available: Experimental details, XAS results, and Tafel plots. See DOI: 10.1039/b000000x/
[‡] Fax: (865) 974-7076; Tel: (865) 974-2421; E-mail: apapandrew@utk.edu

alloy formation observable in the x-ray diffraction spectra, SI Fig. 1;† however, the shifts in the peak position do not match what would be expected if the nanotubes were completely alloyed. A Vegard's law calculation of alloying degree in the PtPdNT samples based on respective shifts of the (111) lattice peaks suggest ~20% alloying. We interpret this to mean that there is interfacial alloying of the separate Pt and Pd phases that occurred after the sequential depositions of the two metals at low temperatures.
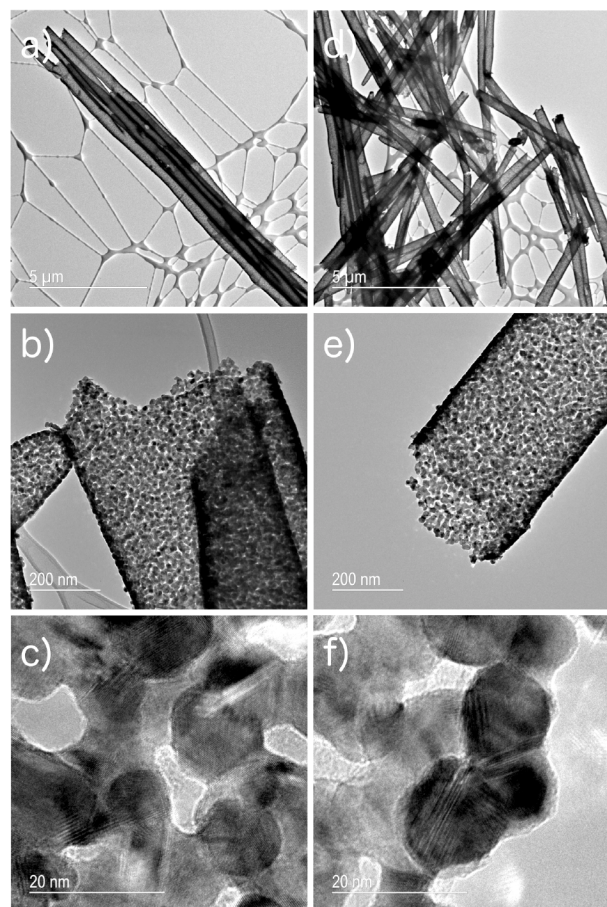
Fig. 1 HR-TEM images of the 10% PtPdNTs (left) and the 13% PtPdNTs (right). The low magnification images (a, d) show the high aspect ratio of the nanotubes, while the nanoscale porosity is most clearly demonstrated in the medium magnification (b, e) and the individual grains/pores in the high magnification images (c, f). Images were obtained following heat treatments in 4% H_2 for 1 hr at 250°C.

Detailed analysis of the EXAFS obtained at the Pt L_3 and Pd K edges (Fig. 2a-b, respectively) also indicates segregation of Pt and Pd within the nanotube wall. X-ray absorption fine structure (XAFS) measurements were performed at room temperature using beamline 20-BM-B of Advanced Photon Source (APS). Bond lengths determined from the Pd-Pd first shell scattering path match those of Pd foil and monometallic Pd nanotubes, suggestive of a highly segregated Pd phase. Pt L_3 EXAFS resolve a distinct Pt-Pd interaction observed in the destructive interference at ~2.5 Å. Analysis of the Pt-Pt, and Pt-Pd first-shell scattering path amplitudes suggest approximately 20% of the Pt is alloyed with Pd (see the atomic coordination, N, in SI Table 1†), in agreement

with the XRD data, while bond lengths in a distinct, Pt-only phase match those of Pt foil. Bond lengths in the mixing zone between the segregated Pt- and Pd-only phases are consistent with a compressed Pt lattice. The EXAFS thus illustrate an isolated Pt phase, a region with Pt-Pd mixing, and an isolated Pd phase where the mixed Pt-Pd zone is a small contributor to the overall structure.
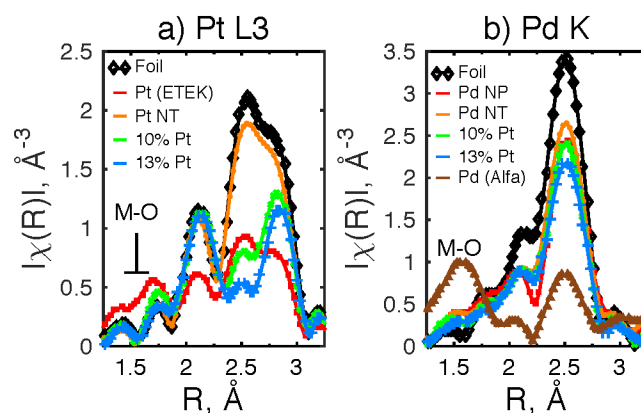
Fig. 2 Forward Fourier transforms of the EXAFS at the Pt L_3 (a) and Pd K (b) edges. Data for the reference foil, the respective pure metal nanotubes, and nanoparticles are included in each figure for comparison. The radial position of the metal-oxygen (M-O) bond is indicated. A distinct destructive interference feature at ~2.5 Å in the Pt L_3 edge EXAFS characterizes Pt-Pd interactions and is definitive in the PtPdNTs.

The EXAFS can also be used to illustrate a decrease in the surface oxide content compared to similarly sized nanoparticle grains with a corresponding increase in metal coordination. The metal-oxygen (M-O) interaction, demarcated on Fig. 2, shows a reduction in the M-O interaction for the nanotubes. These results suggest that the PtPdNTs are more highly coordinated than their isolated nanoparticle analogs. Higher degrees of coordination have been correlated to improved catalyst durability and surface-normalized activity.[36,37,39] This is an advantage of the nanotube form factor in comparison to nanoparticle catalysts.

Additional structural information was obtained by analysis of the x-ray absorption near edge spectra (XANES) at the Pt L_3 edge illustrated in SI Fig. 2.† There is a < 0.4 eV shift of the step-edge to lower energies suggestive of electron transfer from the Pd to the Pt as is predicted from d-band calculations for Pt overlayers atop Pd bulk polycrystals[6,40]. The shift observed here corresponds closely to the expected shift[40] and suggests that we have synthesized a segregated, polycrystalline catalyst homeomorph of the bulk polycrystals previously investigated[6].

Changes in electron filling manifest also as subtle changes in the charging current obtained in N_2-saturated electrolyte, see Fig. 3a. Relative to monometallic Pt NTs, the charging currents of the PtPdNTs illustrate an oxophilic shift of ~0.1 eV in the H-binding energy. This was quantified by observing the rightward shift of the (110) Pt-H oxidation peak at ~0.3 V vs. RHE in Fig. 3a and assuming a Brønsted-Evans-Polanyi relationship for H adsorption[41]. This shift in the H-binding energy to more oxophilic values is also consistent with shifts of the metal oxide reduction region as indicated on Fig. 3a. Because the shift in the oxide reduction region
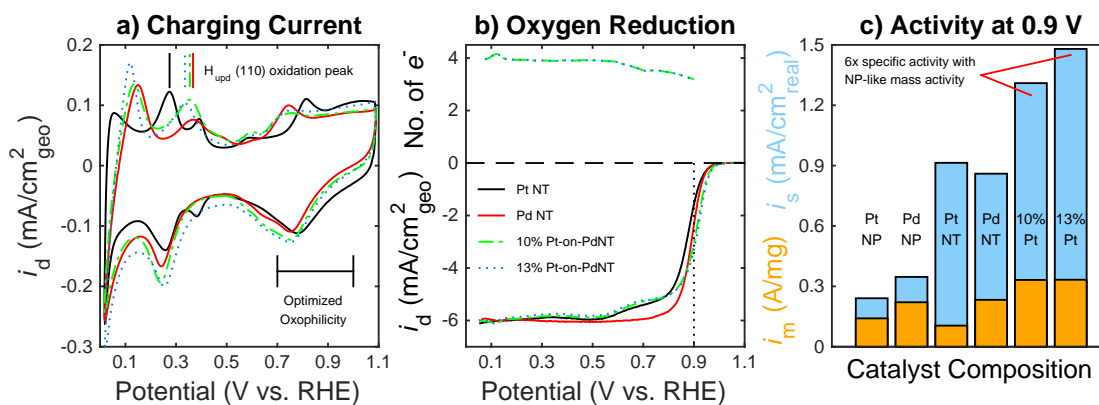
Fig. 3 iR-corrected electrochemical data collected in static, N_2-saturated, 0.1M KOH at 50 mV/s (a) illustrate how the oxophilicity and hydrophilicity of the surface is modulated by composition. As evidenced by changes in both the H_{upd} (110) oxidation peak and the oxide reduction peak, the oxophilicity of the PtPdNTs lies intermediate to the monometallic PtNTs and PdNTs as has been identified as optimum for alkaline ORR. Electrochemical data collected at 1600 rpm in O_2-saturated, 0.1M KOH at 10 mV/s (b) illustrates the oxygen reduction activity of the PtPdNTs. In the transition from low to high current density, the number of electrons transferred is less than 4 for the nanotubes, suggestive of peroxide formation at low overpotential similar to previous observations[7]. The specific and mass activities at 0.9 V vs. RHE have been illustrated (c) for reference carbon-supported catalysts and the nanotubes considered here.

is small, we cannot preclude the possibility that both Pt and Pd surface atoms contribute to the charging current. Consequently, we believe that we will observe combined bi-functional and ligand effects in the oxygen reduction data for segregated Pt clusters on an underlying, exposed Pd support.

The oxygen reduction activity collected from the rotating disk electrode data, given in Fig. 3b-c, illustrate a nearly 6x improvement in surface-area-normalized activity and improvements in mass activity vs. the carbon-supported nanoparticle catalysts. By optimizing the structure of the nanotubes, we have synthesized practical high-surface-area catalysts with comparable surface-normalized activity to bulk single-crystal electrodes. These catalysts have a specific activity of 1.5 mA/cm$^2_{metal}$ at 0.9 V vs. RHE while demonstrating dramatically increased noble metal utilization efficiency: 0.332 A/mg$_{PGM}$ for the optimized nanotube vs. 0.141 A/mg$_{PGM}$ for carbon-supported Pt nanoparticles.

This was achieved for the PtPdNTs despite having a lower surface area (larger grain size) than typical nanoparticles, which we believe is closely related to the nanoporous structure of the tube wall[42]. Activity results, composition, and electrochemically active surface area (ECSA) are summarized in Table 1. Data analysis procedures and the polarization response during Cu stripping are given in the Supplementary Information and in SI Fig. 3†.

Table 1 Catalyst composition, active area, and activity at 0.9 V vs. RHE.

Catalyst	ECSA, m^2/g	i_m, A/mg	i_s, mA/cm^2
Pt NP (ETEK)	58.5	0.141	0.241
Pd NP (Alfa Aesar)	63.7	0.221	0.347
Pd NP	61.0	0.274	0.449
Pt NT	11.5	0.105	0.914
Pd NT	27.1	0.233	0.860
10% PtPdNT	25.3	0.332	1.31
13% PtPdNT	22.5	0.333	1.48

In addition to the increase in activity of the PtPdNTs, there is a mass activity enhancement for the nanoparticles synthesized

using our chemical vapor deposition technique in comparison to both the commercial, carbon-supported Pt NP (ETEK) and Pd NP (Alfa Aesar) catalysts. Such an improvement could be related to the reduced oxophilicity of our Pd NP catalysts as evidenced by the rightward shift in the surface oxide reduction region (see SI Fig. 4†). Such a shift for nanoparticle catalysts is related to changes in the relative distribution of surface active sites, namely (111) vs. (100) vs. stepped (110)-like sites.[7] The Pd NPs that we synthesize also demonstrate a more highly coordinated structure in the EXAFS data in comparison to the commercial catalyst. Such behavior could suggest a higher proportion of close-packed surface sites, thus corroborating the electrochemical charging data.

Kinetic currents and the number of electrons transferred were determined using a Levich-Koutecky analysis[43] by applying Eq. 1 to ORR data collected at 400, 900, 1600, and 2500 rpm.

$$\frac{1}{i} = \frac{1}{0.62nFAD_{O_2}^{\frac{2}{3}}v^{-\frac{1}{6}}C_{O_2}^*\omega^{\frac{1}{2}}} + \frac{1}{i_k} \quad (1)$$

Here, i is the current, i_k is the kinetic current, n is the number of electrons transferred, F is Faraday's constant, D is the diffusion coefficient of O_2 in 0.1M KOH, C^* is the bulk concentration of O_2 in 0.1M KOH, v is the kinematic viscosity of the electrolyte, and ω is the rotation speed of the electrode.[43]

The number of electrons transferred drops from four in the high current density region of the oxygen reduction wave indicating that there is peroxide generation similar to previous observations[7] and may indicate a two-step reduction process[4]. The results for the PtPdNTs in this regard match those for the PtNT.

A Tafel analysis was conducted to investigate changes to the rate-determining step (rds) among the nanotube electrocatalysts. The Tafel slope describes how the current changes with respect to potential and is characteristic of the interfacial reaction kinetics.[43] Consequently, it has been used to hypothesize the rds by comparing it to the results from microkinetic models for differ-

ent ORR mechanisms.[44] The challenge for the ORR is that the interfacial reaction kinetics are closely coupled to the potential-dependent coverage of spectator water, OH_{ads}, and ill-defined surface oxides.[10,44]

The Tafel slope in this regard changes from the oft-observed ∼60 mV/dec. on Pt at low current densities to ∼45 mV/dec. on the PtPdNTs and PdNTs (see SI Fig. 5†). Such a shift would suggest an increase in the potential dependent coverage of OH_{ads} at low current density/overpotential.[10,44] The increased oxophilicity of the surface achieved to optimize the rds (concerted proton/electron transfer) would then have the added effect here of increasing the coverage of OH_{ads} on the surface. It is possible that the increased coverage of OH_{ads} may preferentially form on the more oxophilic Pd vs. the Pt surface atoms thus freeing the Pt surface for oxygen reduction[6]. Optimizing the electronic structure of the noble-metal electrocatalysts for the ORR involves the practical limitation of high surface coverage of spectator species at low overpotential.[10] Future work must focus on reducing the coverage of these spectator species.

In summary, Pd nanotubes were used as homeomorphs of bulk polycrystals to support segregated Pt, resulting in an optimized electronic configuration for alkaline ORR catalysts. Improvements are attributed to electronic effects on the segregated Pt from the underlying Pd support that was assessed by x-ray absorption spectroscopy. Additionally, changes in the M-H binding energy observed in the electrochemical charging currents corresponded to small shifts in the electronic structure consistent with the anticipated change of d-band filling for Pt overlayers on Pd surfaces. Analysis of the electrochemical kinetic currents suggest changes in surface coverage of spectator species that are consistent with changes in the electron structure of the PtPdNTs. The vapor-grown, bi-metallic nanotubes used here have successfully translated the gains typically seen for well-defined overlayers on bulk polycrystals to realizable electrocatalysts.

References

1 J. R. Varcoe, P. Atanassov, D. R. Dekel, A. M. Herring, M. A. Hickner, P. A. Kohl, A. R. Kucernak, W. E. Mustain, K. Nijmeijer, K. Scott, T. Xu and L. Zhuang, *Energy & Environmental Science*, 2014, **7**, 3135–3191.

2 J. S. Spendelow and A. Wieckowski, *Physical Chemistry Chemical Physics*, 2007, **9**, 2654–2675.

3 X. Ge, A. Sumboja, D. Wuu, T. An, B. Li, F. W. T. Goh, T. S. A. Hor, Y. Zong and Z. Liu, *ACS Catalysis*, 2015.

4 H. A. Gasteiger, S. S. Kocha, B. Sompalli and F. T. Wagner, *Applied Catalysis B: Environmental*, 2005, **56**, 9–35.

5 H. Yang and R. L. McCreery, *Journal of The Electrochemical Society*, 2000, **147**, 3420–3428.

6 F. H. B. Lima, J. Zhang, M. H. Shao, K. Sasaki, M. B. Vukmirovic, E. A. Ticianelli and R. R. Adzic, *The Journal of Physical Chemistry C*, 2007, **111**, 404–410.

7 H. Erikson, A. Sarapuu, N. Alexeyeva, K. Tammeveski, J. Solla-Gullón and J. M. Feliu, *Electrochimica Acta*, 2012, **59**, 329–335.

8 M. Pourbaix, *Atlas of electrochemical equilibria in aqueous solutions*, NACE, 1974.

9 J. K. Norskov, J. Rossmeisl, A. Logadottir, L. Lindqvist, J. R. Kitchin, T. Bligaard and H. Jonsson, *Journal of Physical Chemistry B*, 2004, **108**, 17886–17892.

10 S. Gottesfeld, *ECS Transactions*, 2014, **61**, 1–13.

11 S. Gottesfeld, ECS Meeting Abstracts, 2015, p. 1835.

12 N. M. Markovic, ECS Meeting Abstracts, 2015, p. 1836.

13 J. Greeley, I. E. L. Stephens, A. S. Bondarenko, T. P. Johansson, H. A. Hansen, T. F. Jaramillo, J. Rossmeisl, I. Chorkendorff and J. K. Norskov, *Nature Chemistry*, 2009, **1**, 552–556.

14 Y. Hori, A. Murata, K. Kikuchi and S. Suzuki, *Journal of the Chemical Society, Chemical Communications*, 1987, 728–729.

15 I. Katsounaros, W. B. Schneider, J. C. Meier, U. Benedikt, P. U. Biedermann, A. Cuesta, A. A. Auer and K. J. J. Mayrhofer, *Physical Chemistry Chemical Physics*, 2013, **15**, 8058–8068.

16 K. J. P. Schouten, M. J. T. C. van der Niet and M. T. M. Koper, *Physical Chemistry Chemical Physics*, 2010, **12**, 15217–15224.

17 E. Herrero, Q.-S. Chen, J. Hernández, S.-G. Sun and J. M. Feliu, *Physical chemistry chemical physics : PCCP*, 2011, **13**, 16762–16771.

18 T. Hatsukade, K. P. Kuhl, E. R. Cave, D. N. Abram and T. F. Jaramillo, *Physical Chemistry Chemical Physics*, 2014, **16**, 13814–13819.

19 D. Li, C. Wang, D. S. Strmcnik, D. V. Tripkovic, X. Sun, Y. Kang, M. Chi, J. D. Snyder, D. van der Vliet, Y. Tsai, V. R. Stamenkovic, S. Sun and N. M. Markovic, *Energy Environ. Sci.*, 2014, **7**, 4061–4069.

20 R. R. Adzic, J. Zhang, K. Sasaki, M. Vukmirovic, M. Shao, J. Wang, A. Nilekar, M. Mavrikakis, J. Valerio and F. Uribe, *Topics in Catalysis*, 2007, **46**, 249–262.

21 J. S. Spendelow, G. Q. Lu, P. J. A. Kenis and A. Wieckowski, *Journal of Electroanalytical Chemistry*, 2004, **568**, 215–224.

22 J. Zhang, M. B. Vukmirovic, K. Sasaki, A. U. Nilekar, M. Mavrikakis and R. R. Adzic, *Journal of the American Chemical Society*, 2005, **127**, 12480–12481.

23 J. Zhang, Y. Mo, M. B. Vukmirovic, R. Klie, K. Sasaki and R. R. Adzic, *The Journal of Physical Chemistry B*, 2004, **108**, 10955–10964.

24 Z. Duan and G. Wang, *Journal of Physical Chemistry C*, 2013, **117**, 6284–6292.

25 J. Greeley, T. F. Jaramillo, J. Bonde, I. Chorkendorff and J. K. Norskov, *Nature Materials*, 2006, **5**, 909–913.

26 Y. Yamada, K. Miyamoto, T. Hayashi, Y. Iijima, N. Todoroki and T. Wadayama, *Surface Science*, 2013, **607**, 54–60.

27 T. Wadayama, H. Yoshida, K. Ogawa, N. Todoroki, Y. Yamada, K. Miyamoto, Y. Iijima, T. Sugawara, K. Arihara, S. Sugawara and K. Shinohara, *The Journal of Physical Chemistry C*, 2011, **115**, 18589–18596.

28 B. Han, C. E. Carlton, A. Kongkanand, R. S. Kukreja, B. R. Theobald, L. Gan, R. O'Malley, P. Strasser, F. T. Wagner and Y. Shao-Horn, *Energy Environ. Sci.*, 2015, **8**, 258–266.

29 J. Zhang, F. H. B. Lima, M. H. Shao, K. Sasaki, J. X. Wang, J. Hanson and R. R. Adzic, *The Journal of Physical Chemistry B*, 2005, **109**, 22701–22704.

30 J. Zheng, D. a. Cullen, R. V. Forest, J. a. Wittkopf, Z. Zhuang, W. Sheng, J. G. Chen and Y. Yan, *ACS Catalysis*, 2015, **5**, 1468–1474.

31 Q. Lu, G. S. Hutchings, W. Yu, Y. Zhou, R. V. Forest, R. Tao, J. Rosen, B. T. Yonemoto, Z. Cao, H. Zheng, J. Q. Xiao, F. Jiao and J. G. Chen, *Nat Commun*, 2015, **6**, year.

32 S. St. John, P. Boolchand and A. P. Angelopoulos, *Langmuir*, 2013, **29**, 16150–16159.

33 T.-Y. Chen, Y.-T. Liu, H. M. Nguyen, L.-J. Fan, C.-Y. Wu, T.-J. Mark Luo, C.-H. Lee, Y.-W. Yang, T.-C. Wen and T.-L. Lin, *Journal of Materials Chemistry A*, 2013, **1**, 5660–5669.

34 S. St. John, Z. Nan, N. Hu, D. W. Schaefer and A. P. Angelopoulos, *Journal of Materials Chemistry A*, 2013, **1**, 8903–8916.

35 S. St. John, N. Hu, D. W. Schaefer and A. P. Angelopoulos, *Journal of Physical Chemistry C*, 2013, **117**, 7924–7933.

36 R. W. Atkinson, R. R. Unocic, K. A. Unocic, G. M. Veith, T. A. Zawodzinski and A. B. Papandrew, *ACS Applied Materials & Interfaces*, 2015, **7**, 10115–10124.

37 A. B. Papandrew, R. W. Atkinson, G. A. Goenaga, S. S. Kocha, J. W. Zack, B. S. Pivovar and T. A. Zawodzinski, *Journal of The Electrochemical Society*, 2013, **160**, F848–F852.

38 A. B. Papandrew, C. R. I. Chisholm, S. K. Zecevic, G. M. Veith and T. A. Zawodzinski, *Journal of The Electrochemical Society*, 2013, **160**, F175–F182.

39 C. Koenigsmann and S. S. Wong, *Energy & Environmental Science*, 2011, **4**, 1161.

40 A. Ruban, B. Hammer, P. Stoltze, H. L. Skriver and J. K. Norskov, *Journal of Molecular Catalysis A: Chemical*, 1997, **115**, 421–429.

41 J. Durst, A. Siebel, C. Simon, F. Hasche, J. Herranz and H. A. Gasteiger, *Energy & Environmental Science*, 2014, **7**, 2255–2260.

42 M. Nesselberger, M. Roefzaad, R. Fayçal Hamou, P. Ulrich Biedermann, F. F. Schweinberger, S. Kunz, K. Schloegl, G. K. H. Wiberg, S. Ashton, U. Heiz, K. J. J. Mayrhofer and M. Arenz, *Nat Mater*, 2013, **12**, 919–924.

43 A. J. Bard and L. R. Faulkner, *Electrochemical methods: fundamentals and applications*, Wiley, New York, NY, 2006.

44 A. Holewinski and S. Linic, *Journal of The Electrochemical Society*, 2012, **159**, H864–H870.